

RESEARCH

Open Access



Boltzmann- and Non-Boltzmann-Based Thermometers in the First, Second and Third Biological Windows for the SrF₂:Yb³⁺, Ho³⁺ Nanocrystals Under 980, 940 and 915 nm Excitations

Linxuan Wang^{1,2}, Liang Li^{1,2}, Maohui Yuan^{1,2*}, Zining Yang^{1,2,3}, Kai Han^{1,2}, Hongyan Wang^{1,2,3*} and Xiaojun Xu^{1,2,3}

Abstract

Spectrally determination of temperature based on the lanthanide-doped nanocrystals (NCs) is a vital strategy to noninvasively measure the temperature in practical applications. Here, we synthesized a series of SrF₂:Yb³⁺/Ho³⁺ NCs and simultaneously observed the efficient visible upconversion luminescence (UCL) and near-infrared (NIR) downconversion luminescence (DCL) under 980, 940 and 915 nm excitations. Subsequently, these NCs were further utilized for thermometers based on the Boltzmann (thermally coupled levels, TCLs) and non-Boltzmann (non-thermally coupled levels, NTCLs) of Ho³⁺ ions in the first (~ 650 nm), second (~ 1012 nm) and third (~ 2020 nm) biological windows (BW-I, BW-II and BW-III) under tri-wavelength excitations. The thermometric parameters including the relative sensitivity (S_r) and temperature uncertainty (δT) are quantitatively determined on the I_{648}/I_{541} (BW-I), I_{1186}/I_{1012} (BW-II), and I_{1950}/I_{2020} (BW-III) transitions of Ho³⁺ ions in the temperature range of 303–573 K. Comparative experimental results demonstrated that the thermometer has superior performances.

Keywords: NIR luminescence, Non-thermally coupled energy levels, Wide range temperature sensing, Tri-wavelength excitations

Introduction

As a basic physical variable, the temperature is closely related to human life and practical activities. Traditional thermometers possess a relatively large size and need to be physically contacted with the measured object, which severely limits the accuracy of temperature detection and restricts the use of many fields such as biological issues, microelectronic circuits, and nanoscale applications [1]. Therefore, accurate, fast and noninvasive measurement of the temperature is of great significance to

practical applications. Lanthanide-doped NCs based on FIR (fluorescence intensity ratio) or LIR (luminescence intensity ratio) technology could be used as luminescent thermometers which have been extensively developed recently [2–5]. The reason is that lanthanide ions have abundant energy levels and their emissions are heavily dependent on the temperature. These lanthanide-doped luminescent thermometers show the advantages such as fast response, high spatial resolution, high sensitivity, wide adaptability, small error caused by power fluctuation of excitation light source and fluorescence loss [6–10].

Generally, the most present research works have focused on the TCLs of lanthanide ions which the ΔE is limited to 200–2000 cm⁻¹ because this can ensure that

*Correspondence: yuanmaohuino1@126.com; wanghongyan@nudt.edu.cn

¹ College of Advanced Interdisciplinary Studies, National University of Defense Technology, Changsha 410073, China
Full list of author information is available at the end of the article

the two levels are spectrally separated and not too far apart leading to the variation in thermalization is insignificantly observed [11, 12]. Nevertheless, this additional requirement greatly restrains the utility of numerous NTCLs in lanthanide ions. Thus, the thermometers based on the NTCLs, which are no longer restricted to limitation of ΔE and can expand the detection wavelengths in a relatively wide range, can achieve relatively high S_r and low δT and further expand their applications [13–15]. Generally, the quantitative NTCLs model is established by using the Arrhenius equation which can break the restriction of the ΔE between the NTCLs and well predict the FIR and the accuracy of temperature measurement. As is well known, compared to the strong scattering and absorption effects of visible light in biological tissues, the so-called first (BW-I: 650–950 nm), second (BW-II: 950–1700 nm) and third (BW-III: 1700–2500 nm) optically transparent BWs in the range of 650–2500 nm possess strong tissue penetration and have less scattering, low absorption and weak spontaneous luminescence. Hence, the design of a thermometer, which can simultaneously measure the temperature in the BW-I, BW-II and BW-III, has practical significance and needs in biological applications.

Up till now, many lanthanide ions have been used for temperature measurement, including Yb^{3+} and Ho^{3+} ions [16–19]. On the one hand, Yb^{3+} ions have a large absorption cross section, no excited-state absorption, and a wide absorption spectrum (800–1100 nm) and emission spectrum (975–1200 nm) [20, 21]. On the other hand, Ho^{3+} ions have abundant stepped energy levels and can effectively emit luminescence in a wide range from visible to NIR bands when co-doped with Yb^{3+} ions. Generally, the previously reported Ho^{3+} -based thermometers almost utilize the two TCLs of $^5\text{F}_4$ and $^5\text{S}_2$ centered at approximately 540 nm in the visible light based on the Boltzmann theory [22]. In addition, the traditional excitation laser wavelength is 980 nm which could lead to severe heat absorption by the water molecules, thus extremely restraining its application in biological issues. Actually, the Yb^{3+} ions have appreciable absorption capability in other excitation wavelengths (such as 915 nm) where the water absorption coefficient is relatively low. Therefore, exploring the thermometers under different wavelength excitations, especially covering the three biological windows, has very important value in biological applications. However, there still lacks the corresponding research on this aspect [23–25].

In this work, we synthesized a sequence of $\text{SrF}_2:\text{Yb}^{3+}/\text{Ho}^{3+}$ (12/x mol%) NCs doped with different Ho^{3+} concentrations by hydrothermal method. We further investigated the doping Ho^{3+} concentrations dependent on both the UCL and DCL properties, as well as their

mechanism of populations and transitions. Subsequently, the $\text{SrF}_2:\text{Yb}^{3+}/\text{Ho}^{3+}$ (12/0.1 mol%) NCs with the stronger luminescence were selected to study the thermal effect under 980, 940 and 915 nm continuous-wave (CW) lasers with the same pumping power density of 110 W cm^{-2} . In addition, we innovatively investigated the temperature-dependent luminescence based on TCLs and NTCLs simultaneously under tri-wavelength excitations. The quantitative model we used successfully calculated the FIRs and determined the parameters of the thermometer in the first, second and third biological windows.

Experimental Sections

Synthesis of $\text{SrF}_2:\text{Yb}^{3+}/\text{Ho}^{3+}$ NCs

The chemicals of $\text{SrCl}_2 \cdot 6\text{H}_2\text{O}$ (99.99%), $\text{YbCl}_3 \cdot 6\text{H}_2\text{O}$ (99.9%), $\text{HoCl}_3 \cdot 6\text{H}_2\text{O}$ (99.9%), $\text{Na}_3\text{C}_6\text{H}_5\text{O}_7$ (98%) and NH_4F (98%) were purchased from Aladdin (China). The synthesis procedure of NCs by a hydrothermal method is similar to our previous literature [26]. Take $\text{SrF}_2:\text{Yb}^{3+}/\text{Ho}^{3+}$ (12/0.1 mol%) NCs as an example. Firstly, 1.758 mmol SrCl_2 , 0.24 mmol YbCl_3 and 0.002 mmol HoCl_3 were dissolved in 10 mL deionized water and stirred for 1 h. Secondly, 10 mL $\text{Na}_3\text{C}_6\text{H}_5\text{O}_7$ (1 M) and 20 mL NH_4F (1 M) aqueous solutions were added to the above mixed solutions and sequentially stirred for another 1 h. Lastly, the mixtures were transferred into a 50 mL Teflon-lined autoclave and heated at $200 \text{ }^\circ\text{C}$ for 8 h. When the autoclave was naturally cooled down to room temperature, the as-prepared SrF_2 NCs were collected by centrifugation at 6000 rpm for 4 min and washed with ethanol and deionized water several times. The final products were dried in an oven at $60 \text{ }^\circ\text{C}$ for 12 h, and finally, the white powders were obtained for further use.

Characterization

The morphology and size of the as-prepared SrF_2 NCs were characterized by transmission electron microscopy (TEM). X-ray diffraction (XRD) patterns were measured using a powder diffractometer (Bruker D8 advance). The DCL and UCL spectra of $\text{SrF}_2:\text{Yb}^{3+}/\text{Ho}^{3+}$ NCs were measured by a fluorescence spectrophotometer (Zolix Omni-l3072i) coupled with an R928 photomultiplier tube (PMT) for visible light detection and an InGaAs avalanche photodetector (ZPS-PN15) for NIR emissions collection. The excitation sources are semiconductor lasers with different wavelengths of 980, 940, and 915 nm. The UV–Vis–NIR spectra of $\text{SrF}_2:\text{Yb}^{3+}/\text{Ho}^{3+}$ (12/0.1 mol%) NCs were recorded in diffuse reflectance mode in the range of 400–2200 nm by using PerkinElmer Lambda-750 UV–Vis–NIR spectrometer unit. For temperature-dependent luminescence measurement, a temperature controller (RT 600, Shanghai Hotz Instrument

Technology Co., Ltd) was used to change and control the temperature. At room temperature, the spectra in the wavelength range of 400–2200 nm were collected using the constructed experiment system. Then, the sample was heated by the temperature controller, and the spectra were detected with a step of 25 K in the range of 303–573 K. Especially, we set the heating rate of the temperature controller to 12.5 K min⁻¹ and kept the constant temperature for 12 min to ensure that the temperature of sample always reached the scheduled temperature during the spectrum acquisition process.

Results and Discussion

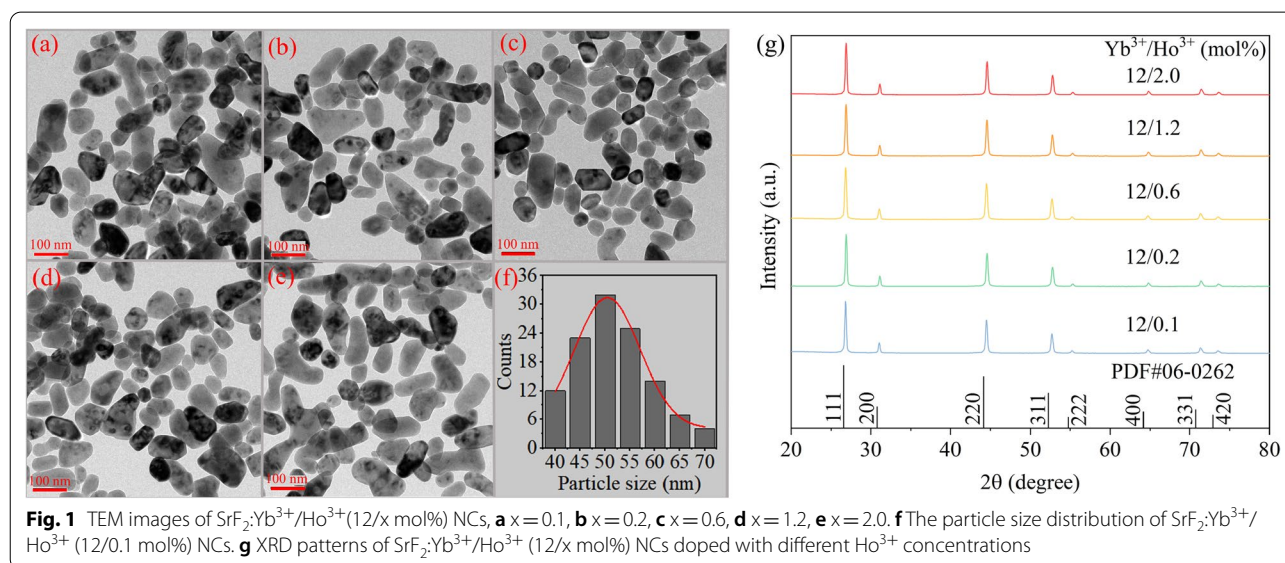
Structure Characterization

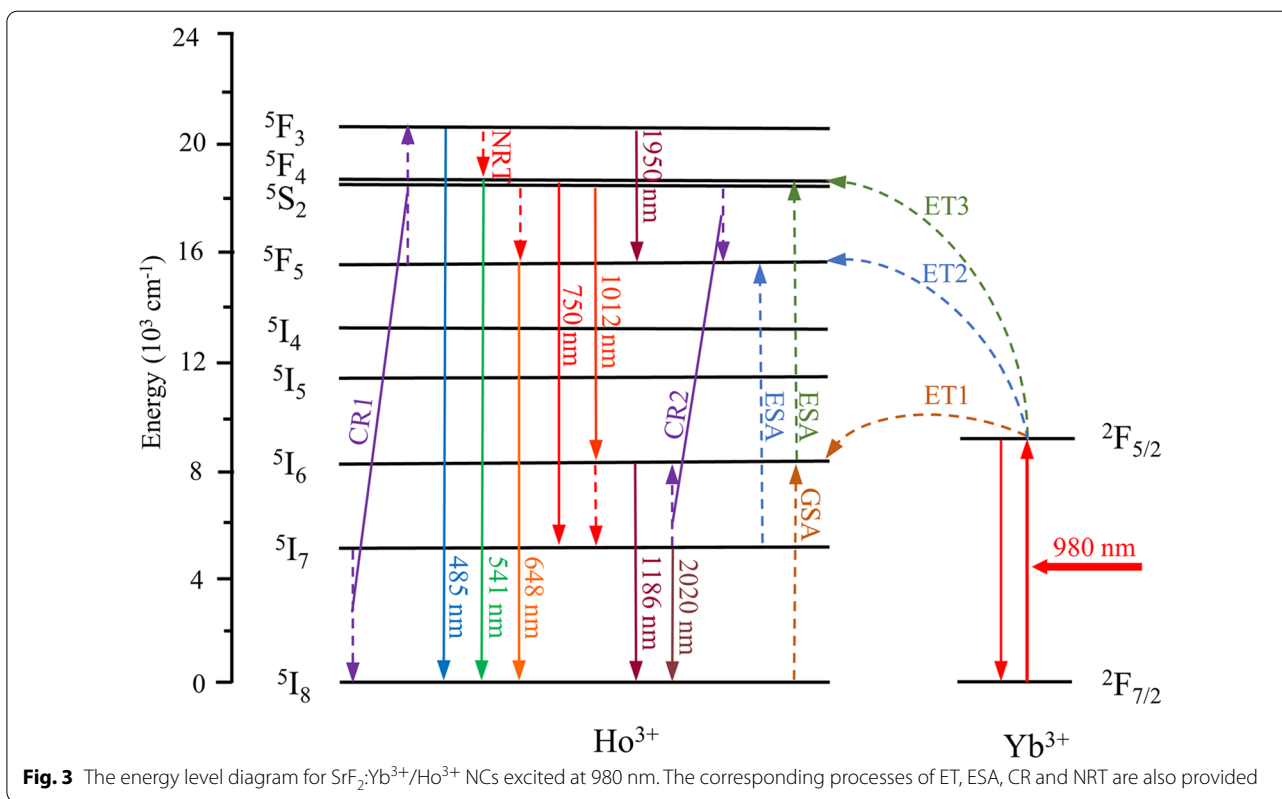
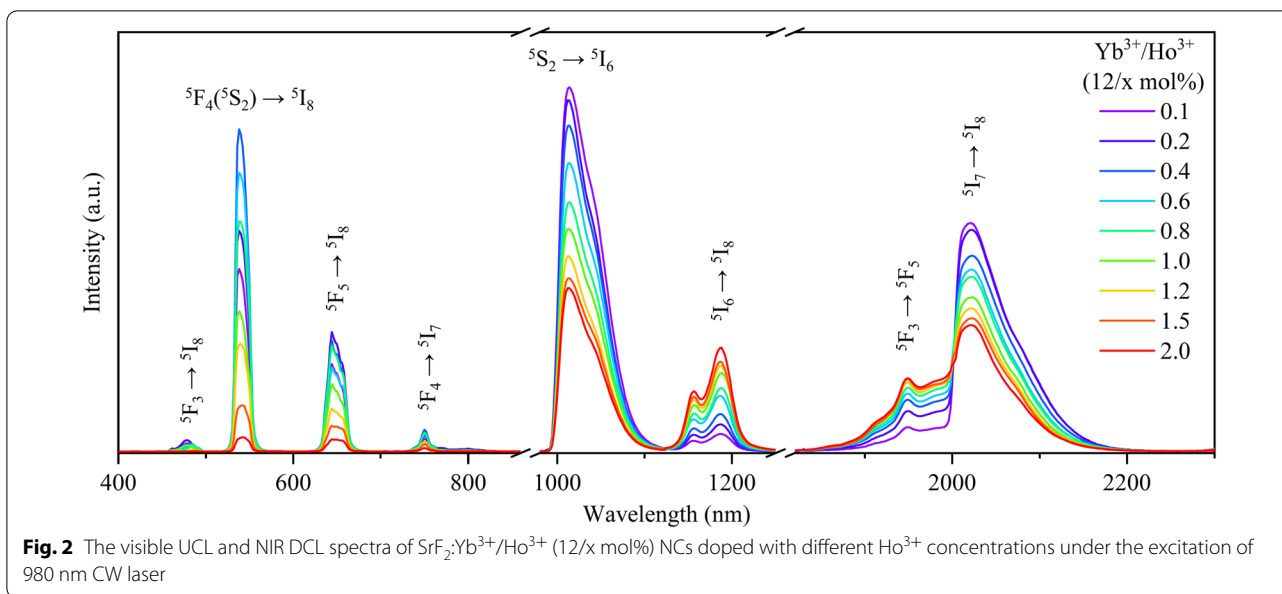
Figure 1a–e shows the TEM images of SrF₂:Yb³⁺/Ho³⁺(12/x mol%) doped with different Ho³⁺ concentrations. The morphology of these NCs exhibits an ellipse or rectangle shape. Figure 1f demonstrates the average size of these synthesized NCs is about 50 nm. As shown in Fig. 1g, XRD patterns further prove that the diffraction peaks of the samples match the standard card of the SrF₂ phase (JCPDS No. 06-0262) well. Both the TEM and XRD characterizations reveal that the doping of small amounts of Yb³⁺ and Ho³⁺ ions has almost no effect on the lattice structure and morphology of the SrF₂ NCs.

DCL and UCL Properties

In our preliminary experiment as shown in Additional file 1: Fig. S1, when the doping concentration of Ho³⁺ was fixed at 0.1 mol%, the intensity of UCL firstly increased and then decreased with the increase in Yb³⁺ concentration. The luminescence intensity reached its maximum when the concentration of Yb³⁺ was

12 mol%. Therefore, the Yb³⁺ concentration was fixed at 12 mol% and further investigated the dependence of the luminescence intensity on Ho³⁺ doping concentration of SrF₂:Yb³⁺/Ho³⁺ (12/x mol%) NCs. Figure 2 shows the visible UCL and NIR DCL spectra of SrF₂:Yb³⁺/Ho³⁺ (12/x mol%) NCs doped with different Ho³⁺ concentrations under the excitation of 980 nm laser. There are eight typical emission bands centered at 485, 541, 648, 750, 1012, 1186, 1950, and 2020 nm, which are ascribed to the transitions of ⁵F₃ → ⁵I₈, ⁵F₄(⁵S₂) → ⁵I₈, ⁵F₅ → ⁵I₈, ⁵F₄ → ⁵I₇, ⁵S₂ → ⁵I₆, ⁵I₆ → ⁵I₈, ⁵F₃ → ⁵F₅ and ⁵I₇ → ⁵I₈ from Ho³⁺ ions, respectively. Obviously, the visible UCL and NIR DCL of SrF₂:Yb³⁺/Ho³⁺ (12/x mol%) NCs exhibit different varying trends when doped with different Ho³⁺ concentration. The visible UCL increases with the increase in Ho³⁺ concentrations within a low concentration range and reaches the maximum at 0.4 mol% Ho³⁺ and then decreases sharply with the increase in Ho³⁺ ions again. Analysis of this phenomenon proves that concentration quenching plays an important role [27]. The increase in Ho³⁺ concentration promotes an increase in rare-earth-ion pair formation in the SrF₂ lattice which correspondingly reduces the distance between Ho³⁺ ions compared the Yb³⁺–Ho³⁺ ions, thus facilitating the occurrence of cross-relaxation (CR) between the adjacent Ho³⁺ ions [28, 29]. For the NIR DCL part, the 1012 and 2020 nm emission intensities gradually decrease with the increase in Ho³⁺ concentration, whereas the 1186 and 1950 nm emission intensities are opposite. We speculate that this is mainly due to the CR process of Ho³⁺ ions (CR1 and CR2 in Fig. 3). The CR1 process of ⁵I₇ + ⁵F₅ → ⁵I₈ + ⁵F₃ can promote the population of





⁵F₃ state and inhibit the population of ⁵I₇ state, which will enhance the 1950 nm emission and decrease the 2020 nm emission, respectively. Similarly, the CR2 process of ⁵I₇ + ⁵S₂ → ⁵I₆ + ⁵F₅ enhances the population of ⁵I₆ state and simultaneously reduces the population of ⁵S₂ state, thus strengthening the 1186 nm emission and

weakening the 1012 nm emission. Notably, the complex excited-state absorption (ESA) and energy transfer (ET) processes can also contribute to the above observed phenomenon.

Figure 3 illustrates the energy level diagram for Yb³⁺ and Ho³⁺ ions under 980 nm excitation, which also

contains the ET, ESA, CR and non-radiative transition (NRT). Generally, Yb^{3+} ions can be populated through the ${}^2\text{F}_{7/2} \rightarrow {}^2\text{F}_{5/2}$ transition by directly absorbing 980 nm photon and then transferring the energy to adjacent Ho^{3+} ions through successive ET processes to populate the ${}^5\text{I}_6$, ${}^5\text{F}_5$ and ${}^5\text{F}_4$ states of Ho^{3+} [30, 31]. Moreover, the ${}^5\text{F}_3$ state is populated by the CR (${}^5\text{I}_7 + {}^5\text{F}_5 \rightarrow {}^5\text{I}_8 + {}^5\text{F}_3$) process, followed generating the 485 nm (${}^5\text{F}_3 \rightarrow {}^5\text{I}_8$) and 1950 nm (${}^5\text{F}_3 \rightarrow {}^5\text{F}_5$) emissions. Subsequently, the electrons in the ${}^5\text{F}_4$ state will transition to the ${}^5\text{I}_8$ and ${}^5\text{I}_7$ states, thereby emitting the 541 nm green light and 750 nm red emission, respectively [32, 33]. Simultaneously, partial electrons in the ${}^5\text{F}_4$ state will populate to the ${}^5\text{S}_2$ state by the NRT process, subsequently transitioning to the ${}^5\text{I}_6$ generating NIR emission at 1012 nm. Similarly, the electrons in the ${}^5\text{F}_5$ state will transition to the ${}^5\text{I}_8$ state, thereby emitting the 648 nm emission. Additionally, the transitions from the ${}^5\text{I}_6$ and ${}^5\text{I}_7$ states to ${}^5\text{I}_8$ state produce the 1186 nm and 2020 nm NIR emissions, respectively.

Notably, except excited by the 980 nm, the Yb^{3+} ions can also be excited at 940 and 915 nm lasers and then transfer energy to Ho^{3+} ions by ET process [34, 35]. To further explore the influence of different excitation sources on the emission spectra for the $\text{SrF}_2:\text{Yb}^{3+}/\text{Ho}^{3+}$ NCs, we further investigate the photoluminescence properties of $\text{SrF}_2:\text{Yb}^{3+}/\text{Ho}^{3+}$ (12/0.1 mol%) NCs under the 980, 940 and 915 nm excitations with the same pumping power density (11 W cm^{-2}), as shown in Fig. 4. The results show that emission efficiency under 980 nm excitation is the highest compared with the 915 and 940 nm excitations, indicating that the largest absorption cross section at 980 nm and lowest absorption cross section at 940 and 915 nm. Under the same pumping power density, the intensity of visible emissions under 980 nm

excitation is almost 40 times than that under 940 nm excitation and 80 times than 915 nm excitation, while the NIR light is almost 4.5 times than that under 940 nm excitation and nine times than that 915 nm excitation. The quantum yields of $\text{SrF}_2:\text{Yb}^{3+}/\text{Ho}^{3+}$ (12/0.1 mol%) NCs were measured under 980 nm excitation which is $\sim 0.51\%$. Unfortunately, we cannot measure the quantum yield of the $\text{SrF}_2:\text{Yb}^{3+}/\text{Ho}^{3+}$ (12/0.1 mol%) NCs under 940 and 915 nm excitations, which is due to the relatively small absorption cross section and much weak luminescence intensity at these two wavelength excitations than that under 980 nm excitation [36–38]. In addition, the size of synthesized $\text{SrF}_2:\text{Yb}^{3+}/\text{Ho}^{3+}$ NCs is about 50 nm, resulting in a large specific surface area which places the dopant lanthanide ions closer to the surface. This leads to an increase in non-radiative relaxations of the emitting and intermediate levels by solvent molecules.

Figure 5a displays the thermal images of $\text{SrF}_2:\text{Yb}^{3+}/\text{Ho}^{3+}$ (12/0.1 mol%) NCs dispersed in ethanol solutions under the 980, 940 and 915 nm laser illustration with a step of 240 s. The excitation power density is 110 W cm^{-1} . Over the 1440 s of the testing process, the temperature gradually rises while manifesting different magnitudes for different excitation wavelengths. Figure 5b further depicts the plot of temperature changes as a function of the heating times. During the heating time, the maximum temperature increases up to 38.5°C and 41.8°C under 915 and 980 nm excitations, respectively. In contrast, the temperature merely elevates from an initial 23.6°C to the final 27.4°C under 940 nm excitation. Obviously, the 940 nm laser-induced heating effect is unobvious compared to the 915 and 980 nm lasers. Therefore, the design of a higher sensitivity thermometer which can minimize thermal effects on organisms has

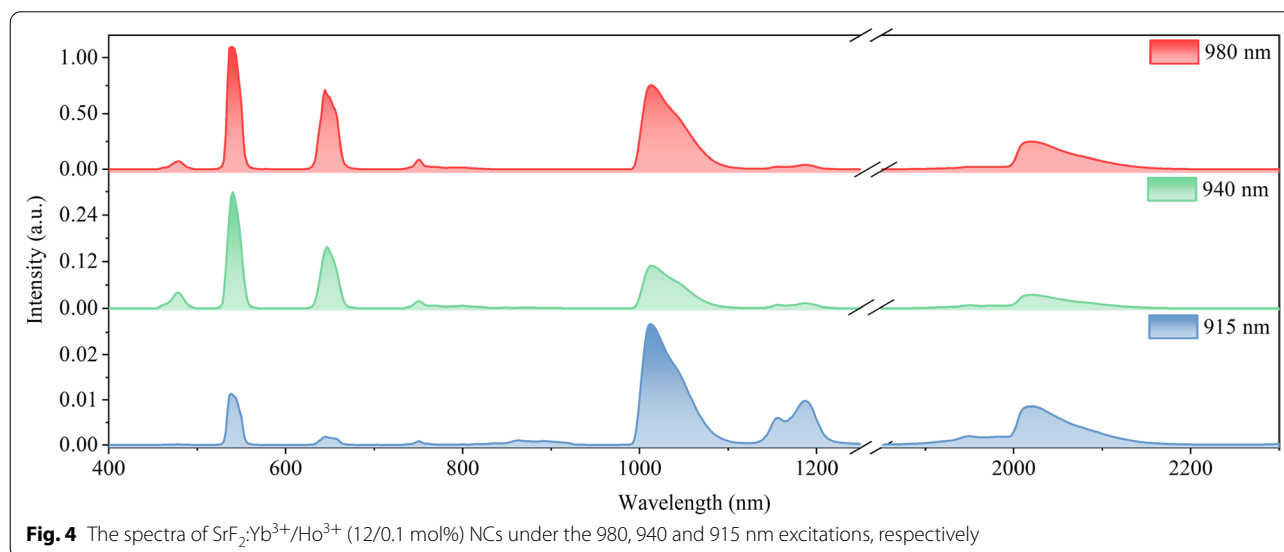
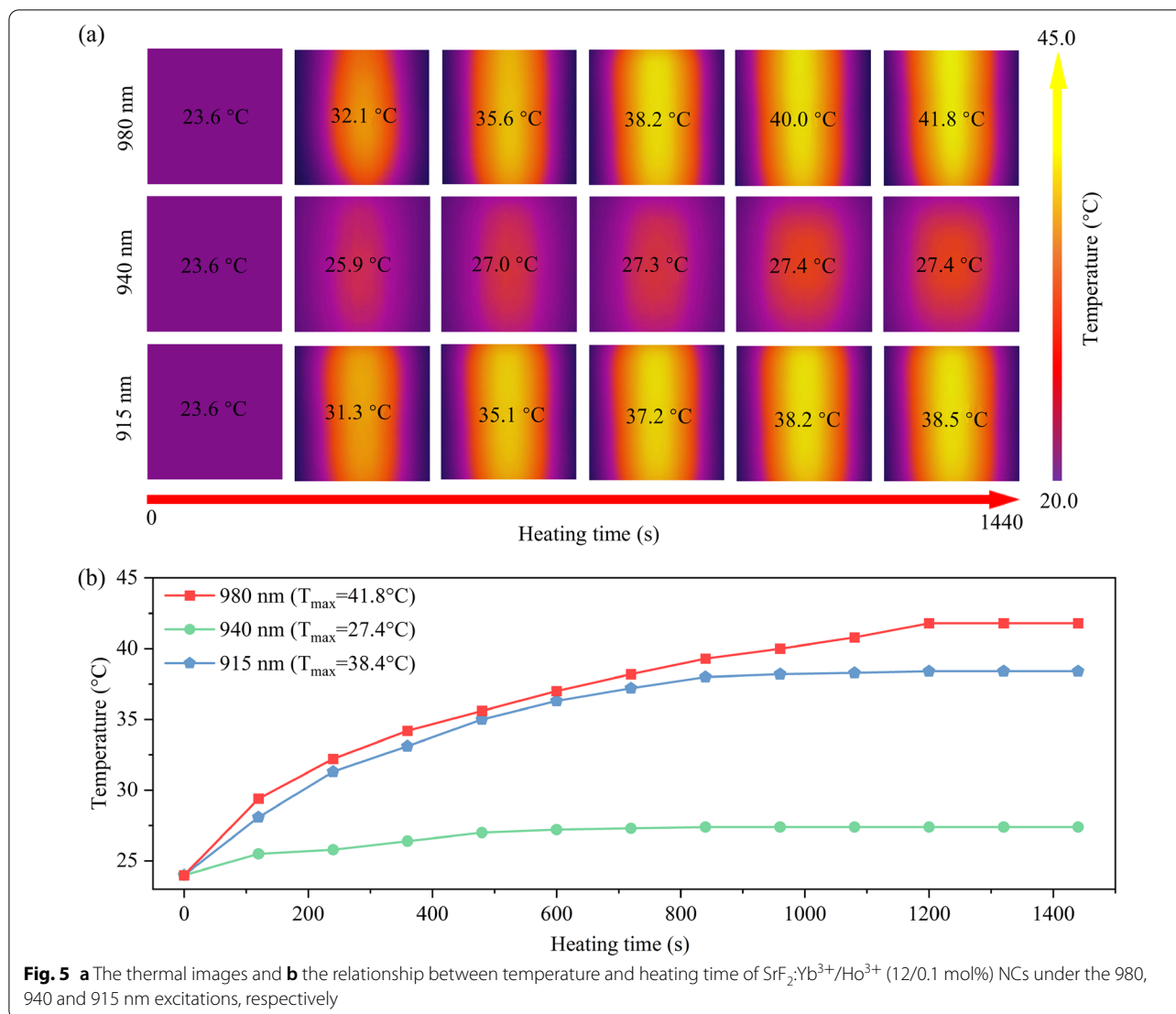


Fig. 4 The spectra of $\text{SrF}_2:\text{Yb}^{3+}/\text{Ho}^{3+}$ (12/0.1 mol%) NCs under the 980, 940 and 915 nm excitations, respectively



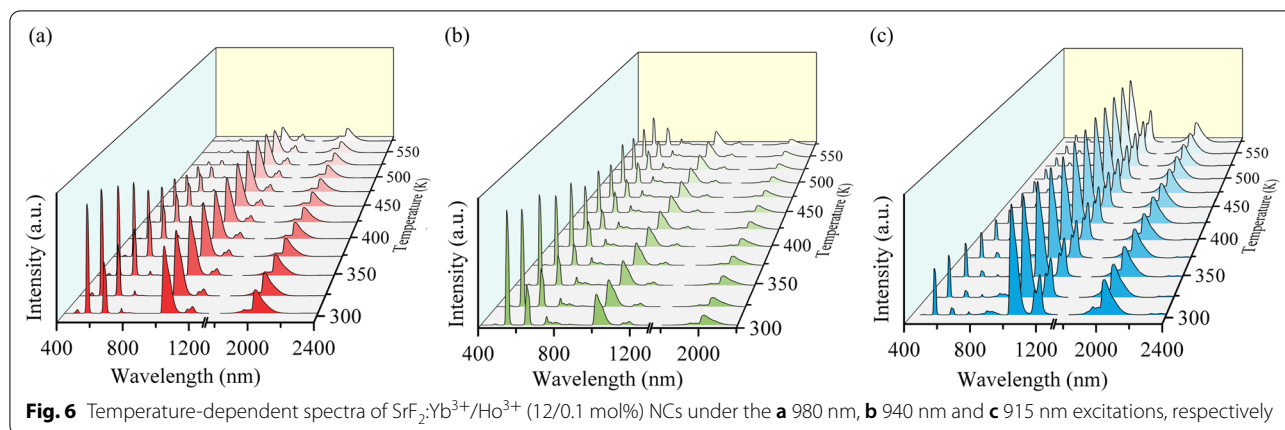
more significant significance in the biological and medical fields.

Ratiometric Temperature Sensing

Having obtained the efficient visible UCL and NIR DCL simultaneously under the excitation of 980, 940 and 915 nm lasers, here, we continue to investigate the ratiometric temperature sensing performances. Figure 6 displays the temperature-dependent spectra of SrF₂:Yb³⁺/Ho³⁺ (12/0.1 mol%) NCs under the excitation of 980, 940 nm and 915 nm in the range of 303–573 K. Both the visible and NIR emissions are decreasing with the increase in temperature. However, the visible UCL thermally quenches more obviously than the NIR DCL. Under the 980 nm excitation, the intensity of visible 541 nm UCL at room temperature (303 K) is about 95

times than that at the highest temperature of 573 K, while red UCL (648 nm) decreases about 16 times from the 303 to 573 K, as shown in Fig. 6a. On the contrary, the NIR DCL has slight changes when the temperature varies from room temperature to 573 K, which possesses a relative highly thermal stability compared with the visible UCL. Particularly, the NIR DCL remains almost unchanged under the 915 nm excitation.

The temperature-dependent spectra ranging from the BW-I, BW-II and BW-III significantly demonstrate that they can be used for detecting the temperature in a wide range. Considering the actual energy levels of Ho³⁺ ions, especially both TCLs and NTCLs emissions, we choose different methods to analyze and calculate the performances of the Boltzmann-based and non-Boltzmann-based thermometers based on the TCLs or NTCLs.



Traditional FIR technology measures the thermal dependence of FIR based on TCLs, which can be defined as follows:

$$\text{FIR}_B = \frac{N_1}{N_2} = \frac{I_1}{I_2} = A \exp\left(-\frac{\Delta E}{KT}\right) \quad (1)$$

where N and I represent the populations of the corresponding energy levels and fluorescence intensity, respectively. A is the constant that depends on the experimental system, T is the absolute temperature and K is the Boltzmann constant.

Arrhenius equation is undoubtedly a good method to analyze the mechanism of temperature sensing behavior when using the NTCLs method, which can be expressed as follows [39]:

$$I(T) = I_0 / \left(1 + B e^{-E_a/KT}\right) \quad (2)$$

where I_0 is the UCL intensity of the measured NCs at room temperature (T_0), $I(T)$ is the UCL intensity at temperature T , B is the constant and E_a is the quenching activation energy. The definition of T and K is the same to Eq. (1).

Although there have been many related studies reported using Arrhenius equation to solve temperature dependence of luminescence intensity due to temperature quenching, in order to further verify the rationality of this equation in dealing with the relationship between Ho³⁺ fluorescence intensity and temperature, we randomly selected the emission intensity centered at 1012 and 2020 nm under 980 nm excitation and obtained the following results through normalization [37, 38]. Additional file 1: Fig. S3a and c shows the dependence of luminescence intensity on the temperature at 1012 nm and 2020 nm, and Additional file 1: Fig. S3b and d displays the fitted results by using Arrhenius equation, respectively. Both the fitting R^2 values, well-fitted Eq. (2), are greater than 99%. The results indicate that the

activation energy is deduced to be 0.27 for 1012 nm and 0.23 eV for 2020 nm, respectively.

Therefore, the FIR based on NTCLs can be modified as follows [40, 41]:

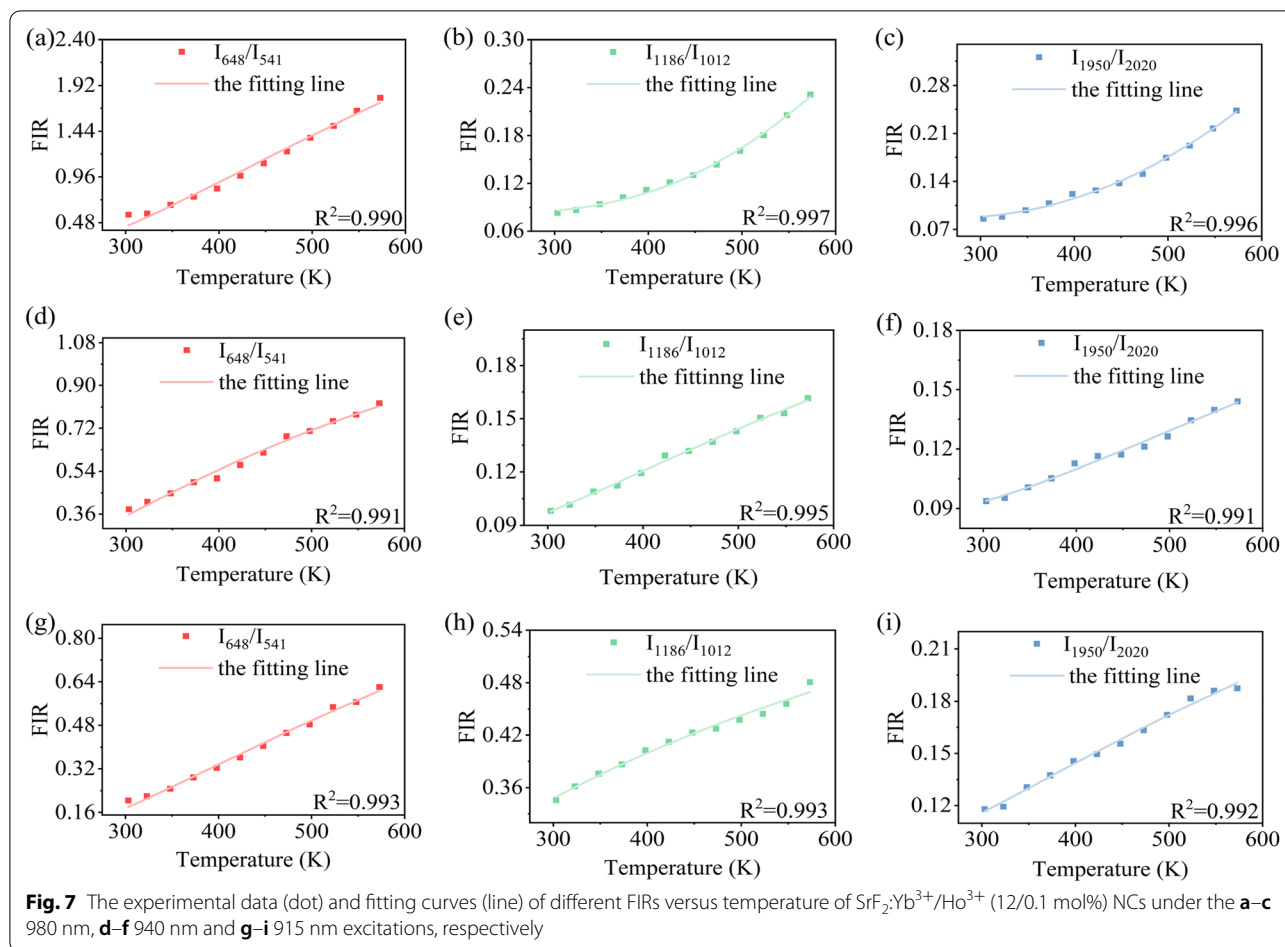
$$\begin{aligned} \text{FIR}_{N-B} &= \frac{I_1(T)}{I_2(T)} = \frac{I_{0,1} 1 + B_2 \exp(-E_2/KT)}{I_{0,2} 1 + B_1 \exp(-E_1/KT)} \\ &\approx \alpha + \beta \exp\left(-\frac{\Delta E_a}{KT}\right) \end{aligned} \quad (3)$$

where $I_1(T)$ and $I_2(T)$ represent the UCL intensity of the two corresponding UCL emissions at temperature T , respectively. α and β are constants that are dependent on I_0 and $I(T)$. E_1 and E_2 are the corresponding quenching activation energy. ΔE_a is a parameter associated with E_1 and E_2 .

Figure 7 shows the FIR ratios of I_{648}/I_{541} , I_{1186}/I_{1012} and I_{1950}/I_{2020} as a function of the external temperature under tri-wavelength excitations. To ensure the accuracy of experimental data, we fitted the FIR ratios using the Gaussian fitting based on the integrated areas of each UCL peak. As a result, the values of FIR increase with the increase in temperature. Among them, the FIR of I_{648}/I_{541} is fitted with Eq. (1), and the FIR of I_{1186}/I_{1012} and I_{1950}/I_{2020} is fitted with Eq. (3). All the fitting R^2 values of curves are greater than 99.0%, indicating that the rationality of the FIR model is based on the TCLs and NTCLs.

To better evaluate the capability of a thermometer, the S_R is used to represent the relative sensitivity of the thermometer, which is defined as follows [42, 43]:

$$S_{R,B} = \frac{1}{\text{FIR}} \left| \frac{\partial \text{FIR}}{\partial T} \right| = \frac{\Delta E}{KT^2} \quad (4)$$



$$S_{R,N-B} = \frac{1}{\text{FIR}} \left| \frac{\partial \text{FIR}}{\partial T} \right| \quad (5)$$

$$= \frac{\Delta E_a}{KT^2} \frac{\beta \exp(-\Delta E_a/KT)}{\alpha + \beta \exp(-\Delta E_a/KT)}$$

Equations (4) and (5) are the expressions S_R based on TCLs and NTCLs, respectively.

Figure 8 displays the relative sensitivity of different FIRs based on TCLs and NTCLs dependent on the temperature. In general, for all the UCL emission ratios, the S_R under 980 nm excitation is the highest, and the S_R under 940 nm excitation is the lowest. Particularly, the maximum S_R of I_{648}/I_{541} based on TCLs reaches 0.94% K⁻¹, 0.57% K⁻¹ and 0.85% K⁻¹ at the room temperature of 303 K under tri-wavelength excitations, and the value S_R decreases gradually with the increase in temperature which is consistent with that described in Eq. (4). It is interesting to note that the maximum S_R of I_{1186}/I_{1012} and I_{1950}/I_{2020} based on NTCLs under 980 nm excitation reaches 0.45% K⁻¹ and 0.40% K⁻¹ at the same temperature of 523 K. And the maximum S_R of I_{1186}/I_{1012} attains 0.23% K⁻¹ at 303 K, whereas

the maximum S_R of I_{1950}/I_{2020} reaches 0.17% K⁻¹ at 398 K under 940 nm excitation. This is because the amplitude of fluorescence intensity varies with temperature under different excitation sources discrepantly, as shown in Fig. 6. In particular, the variation in NIR fluorescence intensity under excitation of 940 and 915 nm is significantly smaller than that under excitation of 980 nm, which leads to a higher relative sensitivity under 980 nm excitation.

For comparison, Table 1 summarizes the performances of our determined thermometers and compared them to the previously reported thermometers related to Ho³⁺ ions. The relatively higher performance can be achieved in the range of 303–573 K for FIRs of I_{648}/I_{541} , I_{1186}/I_{1012} and I_{1950}/I_{2020} in our experiment compared to the previous Ho³⁺-doped thermometers.

In addition to S_R , the temperature uncertainty of δT is a very significant parameter used to evaluate the performance of a thermometer, which is defined as [46]:

$$\delta T = \frac{1}{S_R} \frac{\delta \Delta}{\Delta} \times 100\% \quad (6)$$

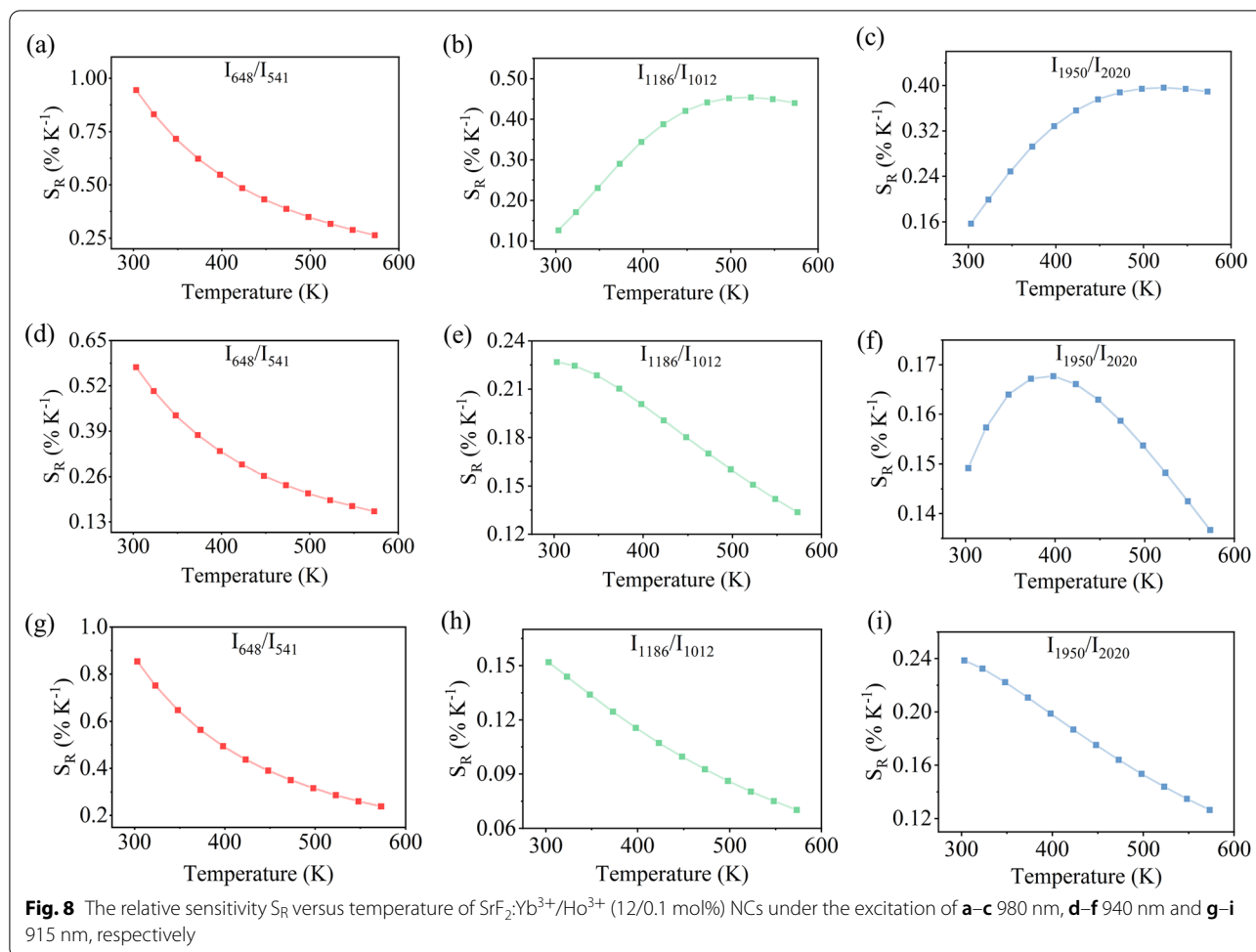
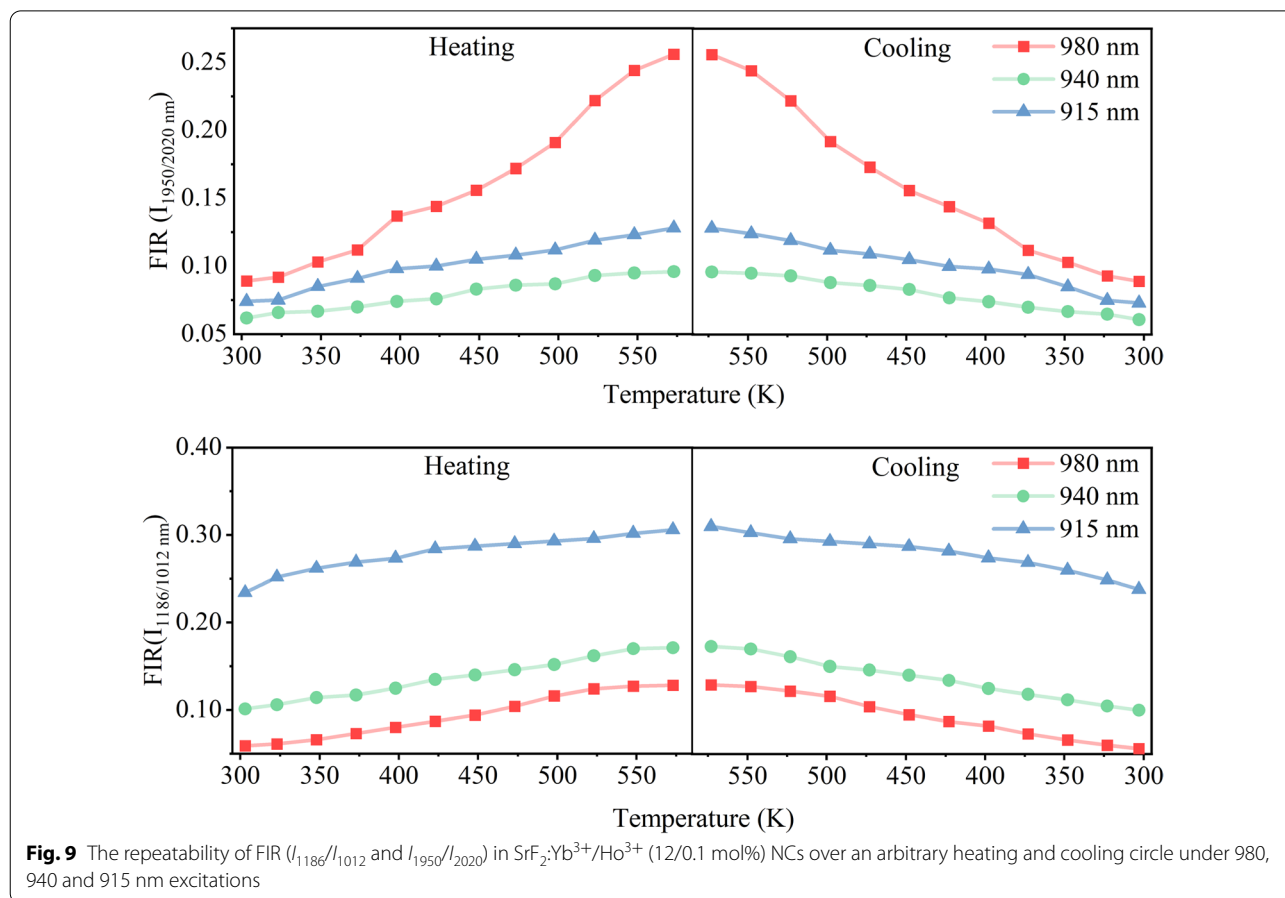


Table 1 The parameters of λ_{ex} , λ_{em} , maximum S_R , temperature range of the Ho^{3+} -doped materials

Samples	λ_{ex} (nm)	λ_{em} (nm)	NTCLs or TCLs	Temperature range (K)	S_R (%·K ⁻¹)	References
$\text{NaYF}_4:\text{Ho}^{3+}$	447	542, 645	TCLs	113–473	0.93 (302 K)	[12]
$\text{BaTiO}_3:\text{Ho}^{3+},\text{Yb}^{3+}$	980	539, 547	TCLs	305–515	0.34 (305 K)	[16]
$\text{LiYF}_4:\text{Yb}^{3+},\text{Ho}^{3+}$	976	655, 546	TCLs	100–500	0.0129 (156 K)	[30]
$\text{BiPO}_4:\text{Yb}^{3+},\text{Ho}^{3+}$	980	652, 657	TCLs	313–573	0.079 (333 K)	[31]
$\text{NBT}:\text{Ho}^{3+},\text{Yb}^{3+}$	980	546, 757	TCLs	93–300	0.29 (93 K)	[41]
$\text{LiYb}(\text{WO}_4)_2:\text{Yb}^{3+},\text{Ho}^{3+}$	980	541, 663	TCLs	298–573	0.7 (300 K)	[44]
$(\text{K}_{0.5}\text{Na}_{0.5})\text{NbO}_3:\text{Ho}^{3+}$	980	526, 552	TCLs	300–650	0.75 (430 K)	[45]
$\text{SrF}_2:\text{Yb}^{3+},\text{Ho}^{3+}$	980	648, 541	TCLs	303–573	0.94 (303 K)	This work
		1186, 1012	NTCLs	303–573	0.45 (523 K)	This work
		1950, 2020	NTCLs	303–573	0.40 (523 K)	This work
	940	648, 541	TCLs	303–573	0.57 (303 K)	This work
		1186, 1012	NTCLs	303–573	0.23 (303 K)	This work
		1950, 2020	NTCLs	303–573	0.17 (398 K)	This work
	915	648, 541	TCLs	303–573	0.85 (303 K)	This work
		1186, 1012	NTCLs	303–573	0.15 (303 K)	This work
		1950, 2020	NTCLs	303–573	0.24 (303 K)	This work



where Δ is the average of measured FIR values in the experiment and $\delta\Delta$ is the uncertainty of the calculated FIR.

Based on Eq. (6), we have calculated the temperature uncertainty of δT for the I_{1950}/I_{2020} . We have obtained the $\delta T < 1.25$ K under 980 nm excitation while $\delta T < 0.96$ K under 915 nm excitation in the temperature range of 303–573 K. In addition, Fig. 9 shows the good repeatability of the temperature-dependent FIR for the NIR bands measured in several heating and cooling circles. The results indicate that the thermometer based on NTCLs of Ho^{3+} has relatively high sensitivity and low temperature uncertainty.

Conclusions

In conclusion, $\text{SrF}_2:\text{Yb}^{3+}/\text{Ho}^{3+}$ (12/ x mol%) NCs with an average size of ~ 50 nm were synthesized through the hydrothermal method and characterized by TEM and XRD. Both the efficient NIR DCL and visible UCL are observed under 980, 940 and 915 nm excitations. The doping Ho^{3+} concentrations dependent on the UCL and DCL, as well as their mechanism of population processes and emission transitions,

are also discussed. Subsequently, the $\text{SrF}_2:\text{Yb}^{3+}/\text{Ho}^{3+}$ (12/0.1 mol%) NCs exhibited the most intense NIR DCL and visible UCL. Then, these NCs were selected to achieve the Boltzmann- and non-Boltzmann-based thermometers under 980, 940 and 915 nm excitations. The obtained maximum S_R of I_{648}/I_{541} based on TCLs is $0.94\% \text{ K}^{-1}$ at 303 K, as well as the $0.45\% \text{ K}^{-1}$ for I_{1186}/I_{1012} and $0.40\% \text{ K}^{-1}$ for I_{1950}/I_{2020} at 523 K based on NTCLs under 980 nm excitation. The results reveal that these NCs can be applied in biological issues to measure the temperature under different laser wavelength excitations and wide emission bands centered in the first, second and third biological windows.

Abbreviations

NCs: Nanocrystals; UCL: Upconversion luminescence; DCL: Downconversion luminescence; NIR: Near-infrared; TCLs: Thermally coupled levels; NTCLs: Non-thermally coupled levels; BW-I: First biological windows; BW-II: Second biological windows; BW-III: Third biological windows; CW: Continuous-wave; TEM: Transmission electron microscopy; XRD: X-ray diffraction; PMT: Photomultiplier tube; CR: Cross-relaxation; ESA: Excited-state absorption; ET: Energy transfer; NRT: Non-radiative transition.

Supplementary Information

The online version contains supplementary material available at <https://doi.org/10.1186/s11671-022-03718-z>.

Additional file 1: Fig. S1. Variation of upconversion emission intensity as a function of Yb³⁺ dopant concentration when fixed the concentration of Ho³⁺ (0.1 mol%). **Fig. S2.** The UV–vis–NIR absorption spectra of SrF₂:Yb³⁺/Ho³⁺ (12/0.1 mol%) NCs. **Fig. S3.** The dependence of luminescence intensity at (a) 1012 nm and (c) 2020 nm of SrF₂:Yb³⁺/Ho³⁺ NCs on the temperature under 980 nm excitation. Arrhenius equation is used to fit the luminescence intensity dependent on temperature at (b) 1012 nm and (d) 2020 nm.

Acknowledgements

Not applicable.

Author contributions

LW and MY contributed to the design of this research. LW and MY carried out the experiments. LW, KH and LL contributed to the data analysis. LW and HW provided the optical spectrum test and measurement. LW and MY wrote the draft of the manuscript. HW and XX revised and finalized the manuscript. All authors have read and approved the final manuscript.

Funding

Not applicable.

Availability of data and material

The datasets used and/or analyzed during the current study are available from the corresponding author on reasonable request.

Declarations

Ethics approval and consent to participate

Not applicable.

Consent for publication

Not applicable.

Competing interests

The authors declare that they have no competing interests.

Author details

¹College of Advanced Interdisciplinary Studies, National University of Defense Technology, Changsha 410073, China. ²State Key Laboratory of Pulsed Power Laser Technology, National University of Defense Technology, Changsha 410073, China. ³Hunan Provincial Key Laboratory of High Energy Laser Technology, National University of Defense Technology, Changsha 410073, China.

Received: 30 June 2022 Accepted: 22 August 2022

Published online: 30 August 2022

References

- Van Swieten TP, Yu DC, Yu T, Vonk SJW, Suta M, Zhang QY, Meijerink A, Rabouw FT (2021) A Ho³⁺-based luminescent thermometer for sensitive sensing over a wide temperature range. *Adv Opt Mater* 9:2001518
- Li D, Mo J, Wang C, Liu W, Ge H, Han D, Hao A, Chai B, She J (2020) Screen printing of upconversion NaYF₄:Yb³⁺/Eu³⁺ with Li⁺ doped for anti-counterfeiting application. *Chin Opt Lett* 18:110501
- Yu B, Zheng B, Xia H, Wang J, Song H, Chen B (2021) Tunable emission and temperature sensing performance in novel oxyfluoride borosilicate glass ceramics containing Eu³⁺/Tb³⁺:KY₃F₁₀ nanocrystals. *Ceram Int* 47:9668–9678
- Yang X, Wang L, Wang R, Yang Z, Song C, Yuan M, Han K, Lan S, Wang H, Xu X (2021) Achieving tunable multicolor display and sensitive temperature sensing in self-sensitization of erbium-doped CaF₂ nanocrystals under 808, 980 and 1532 nm irradiation. *Opt Mater Express* 11:2514–2527
- Periša J, Đorđević V, Ristić Z, Medić M, Kuzman S, Antić Ž, Dramićanin MD (2022) Highly sensitive temperature reading from intensity ratio of Eu³⁺ and Mn⁴⁺ emissions in Y₃A₁₅O₁₂ nanocrystals. *Mater Res Bull* 149:111708
- Gao G, Busko D, Kauffmann-Weiss S, Turshatov A, Howard IA, Richards BS (2018) Wide-range non-contact fluorescence intensity ratio thermometer based on Yb³⁺/Nd³⁺ co-doped La₂O₃ microcrystals operating from 290 to 1230 K. *J Mater Chem C* 6:4163–4170
- Zhong J, Chen D, Peng Y, Lu Y, Chen X, Li X, Ji Z (2018) A review on nano-structured glass ceramics for promising application in optical thermometry. *J Alloy Compd* 763:34–48
- Dong H, Du S, Zheng X, Lyu GM, Sun L, Li L, Zhang P, Zhang C, Yan C (2015) Lanthanide nanoparticles: from design toward bioimaging and therapy. *Chem Rev* 115:10725–10815
- Mancic L, Djukic-Vukovic A, Dinic I, Nikolic MG, Rabasovic MD, Krmpot AJ, Costa AMLM, Trisic D, Lazarevic M, Mojovic L, Milosevic O (2018) NIR photo-driven upconversion in NaYF₄:Yb, Er/PLGA particles for in vitro bioimaging of cancer cells. *Mat Sci Eng C* 91:597–605
- Kibrisli O, Erol E, Vahedigharehchopogh N, Yousef ES, Çelikbilek-Ersundu M, Ersundu AE (2020) Noninvasive optical temperature sensing behavior of Ho³⁺ and Ho³⁺/Er³⁺ doped tellurite glasses through up and down-converted Emissions. *Sens Actuat A* 315:112321
- Cheng Y, Gao Y, Lin H, Huang F, Wang Y (2018) Strategy design for ratiometric luminescence thermometry: circumventing the limitation of thermally coupled levels. *J Mater Chem C* 6:7462–7478
- Xu H, Yang Y, Lu L, Yang Y, Zhang Z, Zhao C, Zhang F, Fan Y (2022) Orthogonal multiplexed NIR-II imaging with excitation-selective lanthanide-based nanoparticles. *Anal Chem* 94:3661–3668
- Wang C, Jin Y, Zhang R, Yao Q, Hu Y (2022) A review and outlook of ratiometric optical thermometer based on thermally coupled levels and non-thermally coupled levels. *J Alloy Compd* 894:162494
- Liu S, Cui J, Jia J, Fu J, You W, Zeng Q, Yang Y, Ye X (2019) High sensitive Ln³⁺/Tm³⁺/Yb³⁺ (Ln³⁺ = Ho³⁺, Er³⁺) tri-doped Ba₃Y₂O₉ upconverting optical thermometric materials based on diverse thermal response from non-thermally coupled energy levels. *Ceram Int* 45:1–10
- Ran WG, Noh HM, Park SH, Lee BR, Kim JH, Jeong JH, Shi JS (2019) Application of thermally coupled energy levels in Er³⁺ doped CdMoO₄ phosphors: enhanced solid-state lighting and non-contact thermometry. *Mater Res Bull* 117:63–71
- Singh P, Yadav RS, Singh P, Rai SB (2021) Upconversion and downshifting emissions of Ho³⁺-Yb³⁺ co-doped ATiO₃ perovskite phosphors with temperature sensing properties in Ho³⁺-Yb³⁺ co-doped BaTiO₃ phosphor. *J Alloy Compd* 855:157452
- Marciniak L, Elzbiaciak-Piecka K, Kniec K, Bednarkiewicz A (2020) Assessing thermometric performance of Sr₂CeO₄ and Sr₂CeO₄:Ln³⁺ (Ln³⁺ = Sm³⁺, Ho³⁺, Nd³⁺, Yb³⁺) nanocrystals in spectral and temporal domain. *Chem Eng J* 388:124347
- Pominova D, Proydakova V, Romanishkin I, Ryabova A, Kuznetsov S, Uvarov O, Fedorov P, Loschenov V (2020) Temperature sensing in the short-wave infrared spectral region using core-shell NaGdF₄:Yb³⁺, Ho³⁺, Er³⁺@NaYF₄ nanothermometers. *Nanomaterials* 10:1992
- Pushpendra KRK, Kalia R, Naidu BS (2020) Upconversion luminescence properties of NaBi(MoO₄)₂:Ln³⁺, Yb³⁺ (Ln = Er, Ho) nanomaterials synthesized at room temperature. *Ceram Int* 46:18614–18622
- Wu Q, Xu Z, Wageh S, Al-Ghamdi A, Zhao S (2021) The dynamic variation of upconversion luminescence dependent on shell Yb³⁺ contents in NaYF₄:Yb³⁺, Tm³⁺@NaYF₄:Yb³⁺, Er³⁺ nanoparticles. *J Alloy Compd* 891:162067
- Wei W, Zhang Y, Chen R, Goggi J, Ren N, Huang L, Bhakoo KK, Sun HD, Tan TTY (2014) Cross relaxation induced pure red upconversion in activator- and sensitizer-rich lanthanide nanoparticles. *Chem Mater* 26:5183–5186
- Li Z, Lin L, Feng Z, Huang L, Wang Z, Zheng Z (2021) Wide-range temperature sensing of NaYF₄:Ho³⁺ nanoparticles by multi-emissions in dual spectral ranges. *J Lumin* 232:117873
- Fan Q, Zhang G, Peng B (2021) Tumor imaging of a novel Ho³⁺-based biocompatible NIR fluorescent fluoride nanoparticle. *J Lumin* 235:118007
- Leal JJ, Rodríguez E, Nava-Dino CG, Maldonado-Orozco MC, Gaxiola F, NarroGarcía R (2021) Effect of Ho³⁺ concentration on the luminescent and thermal stability of tellurite glasses. *Mater Res Bull* 144:111483

25. Gao W, Wang B, Han Q, Gao L, Wang Z, Sun Z, Zhang B, Dong J (2020) Multicolor upconversion emission of Ho^{3+} in single NaYF_4 microrod. *J Alloy Compd* 818:152934
26. Wang L, Yang X, Yuan M, Yang Z, Han K, Wang H, Xu X (2022) Determination of near-infrared downconversion emission of Yb^{3+} and optical temperature sensing performances in Nd^{3+} -sensitized SrF_2 nanocrystals. *Opt Mater* 123:0925–3467
27. Yu X, Zhao T, Wang T, Bao W, Zhang H, Su C (2021) Up-conversion luminescence properties of Ho^{3+} - Yb^{3+} co-doped transparent glass ceramics containing $\text{Y}_2\text{Ti}_2\text{O}_7$. *J Non-Cryst Solids* 574:121163
28. Karthickraja D, Kumar GA, Sardar DK, Karthi S, Dannangoda GC, Martirosyan KS, Prasath M, Gowri M, Girija EK (2021) Fabrication of Nd^{3+} and Yb^{3+} doped NIR emitting nano fluorescent probe: a candidate for bioimaging applications. *Mater Sci Eng C* 125:112095
29. Cao C, Xue M, Zhu X, Yang P, Feng W, Li F (2017) Energy transfer highway in Nd^{3+} -sensitized nanoparticles for efficient near-infrared bioimaging. *ACS Appl Mater Interfaces* 9:18540–18548
30. Li W, Hu L, Chen W, Sun S, Guzik M, Boulon G (2021) The effect of temperature on green and red upconversion emissions of $\text{LiYF}_4:\text{20Yb}^{3+}, 1\text{Ho}^{3+}$ and its application for temperature sensing. *J Alloy Compd* 866:158813
31. Wan N, Fu Z, Wei Y, Sheng T (2019) Investigation for the upconversion luminescence and temperature sensing mechanism based on $\text{BiPO}_4:\text{Yb}^{3+}, \text{RE}^{3+}$ ($\text{RE}^{3+} = \text{Ho}^{3+}, \text{Er}^{3+}$ and Tm^{3+}). *J Alloy Compd* 772:371–380
32. Mondal M, Rai VK (2018) Ho^{3+} - $\text{Yb}^{3+}:\text{YMoO}_4$ core@shell nanoparticles for enhanced visible upconversion and security applications. *J Alloy Compd* 750:304–311
33. Soni AK, Rai VK (2014) $\text{BaZnLa}_2\text{O}_5:\text{Ho}^{3+}$ - Yb^{3+} phosphor for display and security ink application. *J Opt Soc Am B* 31:2201–2207
34. Sun Y, Yang Z, Xie C, Jiang Z (2012) Preparation and characteristics of core-shell structure $\text{Y}_3\text{Al}_5\text{O}_{12}:\text{Yb}^{3+}/\text{SiO}_2$ nanoparticles. *J Alloy Compd* 528:1–9
35. Zhan Q, Qian J, Liang H, Somsfalean G, Wang D, He S, Zhang Z, Andersson-Engels S (2011) Using 915 nm laser excited $\text{Tm}^{3+}/\text{Er}^{3+}/\text{Ho}^{3+}$ -doped NaYbF_4 upconversion nanoparticles for in vitro and deeper in vivo bioimaging without overheating irradiation. *ACS Nano* 5:3744–3757
36. Pilch A, Wawrzyńczyk D, Kurnatowska M, Czaban B, Samoć M, Strek W, Bednarkiewicz A (2017) The concentration dependent up-conversion luminescence of Ho^{3+} and Yb^{3+} co-doped $\beta\text{-NaYF}_4$. *J Lumin* 182:114–122
37. Su J, Zhang X, Li X (2019) Hydrothermal synthesis and green upconversion luminescence of Yb^{3+} and Ho^{3+} co-doped $\text{SrGd}_2(\text{WO}_4)_2(\text{MoO}_4)_2$ nanocrystal. *AIP Adv* 9:125246
38. Boyer JC, van Veggel FCM (2010) Absolute quantum yield measurements of colloidal $\text{NaYF}_4:\text{Er}^{3+}, \text{Yb}^{3+}$ upconverting nanoparticles. *Nanoscale* 2:1417–1419
39. Rodríguez-Díaz JM, Santos-Martín MT (2009) Study of the best designs for modifications of the Arrhenius equation. *Chemom Intell Lab Syst* 95:199–208
40. Li P, Jia M, Liu G, Zhang A, Sun Z, Fu Z (2019) Investigation on the fluorescence intensity ratio sensing thermometry based on nonthermally coupled levels. *ACS Appl Bio Mater* 2:1732–1739
41. Lu Z, Li K, Wang J, Luo L (2021) Photochromic and temperature sensing properties of Ho^{3+} - Yb^{3+} codoped $\text{Bi}_{0.495-x}\text{Na}_{0.5}\text{TiO}_3$ ceramics. *Opt Mater* 111:110718
42. Ćirić A, Stojadinović S, Dramićanin MD (2020) Luminescence temperature sensing using thin-films of undoped Gd_2O_3 and doped with Ho^{3+} , Eu^{3+} and Er^{3+} prepared by plasma electrolytic oxidation. *Ceram Int* 46:23223–23231
43. Kaczmarek AM, Suta M, Rijckaert H, Swieten TPV, Driessche IV, Kaczmarek MK, Meijerink A (2021) High temperature (nano) thermometers based on $\text{LiLuF}_4:\text{Er}^{3+}, \text{Yb}^{3+}$ nano- and microcrystals confounded results for core-shell nanocrystals. *J Mater Chem C* 9:3589–3600
44. Yun X, Zhou J, Zhu Y, Li X, Xu D (2021) Up-conversion luminescence and optical temperature sensing properties of Ho^{3+} -doped double-tungstate $\text{LiYb}(\text{WO}_4)_2$ phosphors. *J Mater Sci Mater Electron* 32:17990–18001
45. Wu X, Lin J, Chen P, Liu C, Lin M, Lin C, Luo L, Zheng X (2019) Ho^{3+} -doped (K, Na) Nb_3O_{10} -based multifunctional transparent ceramics with superior optical temperature sensing performance. *J Am Ceram Soc* 102:1249–1258
46. Savchuk OA, Carvajal JJ, Brites CDS, Carlos LD, Aguiló M, Díaz F (2018) Upconversion thermometry: a new tool to measure the thermal resistance of nanoparticles. *Nanoscale* 10:6602–6610

Publisher's Note

Springer Nature remains neutral with regard to jurisdictional claims in published maps and institutional affiliations.

Submit your manuscript to a SpringerOpen® journal and benefit from:

- Convenient online submission
- Rigorous peer review
- Open access: articles freely available online
- High visibility within the field
- Retaining the copyright to your article

Submit your next manuscript at ► [springeropen.com](https://www.springeropen.com)
